6-1-2018

Charge transfer dynamical processes at graphene-transition metal oxides/electrolyte interface for energy storage: Insights from in-situ Raman spectroelectrochemistry

S. Gupta

S. B. Carrizosa

J. Jasinski

N. Dimakis

Recommended Citation

S. Gupta, et. al., (2018) Charge transfer dynamical processes at graphene-transition metal oxides/electrolyte interface for energy storage: Insights from in-situ Raman spectroelectrochemistry.AIP Advances8:6. DOI: http://doi.org/10.1063/1.5028412

AIP ADVANCES **8**, 065225 (2018)

Charge transfer dynamical processes at graphene-transition metal oxides/electrolyte interface for energy storage: Insights from in-situ Raman spectroelectrochemistry

S. Gupta,[1,a] S. B. Carrizosa,[2] J. Jasinski,[3] and N. Dimakis[4]
[1]*Department of Physics and Astronomy, Western Kentucky University,*
1906 College Heights Blvd, Bowling Green, KY 42101, USA
[2]*Department of Chemistry, Western Kentucky University, 1906 College Heights Blvd,*
Bowling Green, KY 42101, USA
[3]*Department of Chemical Engineering and Conn Center for Renewable Energy Research,*
University of Louisville, KY 40292, USA
[4]*Department of Physics and Astronomy, The University of Texas Rio Grande Valley,*
TX 78539, USA

(Received 10 March 2018; accepted 19 June 2018; published online 29 June 2018)

Hybrids consisting of supercapacitive functionalized graphene (graphene oxide; GO reduced graphene oxide; rGO multilayer graphene; MLG, electrochemically reduced GO; ErGO) and three-dimensional graphene scaffold (rGO$_{HT}$; hydrothermally prepared) decorated with cobalt nanoparticles (CoNP), nanostructured cobalt (CoO and Co_3O_4) and manganese (MnO_2) oxide polymorphs, assembled electrochemically facilitate chemically bridged interfaces with tunable properties. Since Raman spectroscopy can capture variations in structural and chemical bonding, Raman spectroelectrochemistry in operando *i.e.* under electrochemical environment with applied bias is employed to 1) probe graphene/metal bonding and dynamic processes, 2) monitor the spectral changes with successive redox interfacial reactions, and 3) quantify the associated parameters including type and fraction of charge transfer. The transverse optical (TO) and longitudinal optical (LO) phonons above 500 cm^{-1} belonging to Co_3O_4, CoO, MnO_2 and carbon-carbon bonding occurring at 1340 cm^{-1}, 1590 cm^{-1} and 2670 cm^{-1} belonging to D, G, and 2D bands, respectively, are analyzed with applied potential. Consistent variation in Raman band position and intensity ratio reveal structural modification, combined charge transfer due to localized orbital re-hybridization and mechanical strain, all resulting in finely tuned electronic properties. Moreover, the heterogeneous basal and edge plane sites of graphene nanosheets in conjunction with transition metal oxide 'hybrids' reinforce efficient surface/interfacial electron transfer and available electronic density of states near Fermi level for enhanced performance. We estimated the extent and nature ($n-$ or $p-$) of charge transfer complemented with Density Functional Theory calculations affected by hydration and demonstrate the synergistic coupling between graphene nanosheets and nanoscale cobalt (and manganese) oxides for applied electrochemical applications.
https://doi.org/10.1063/1.5028412

I. INTRODUCTION

Intense research and development in clean and sustainable energy sources are stimulated by increasing global demand of electrical energy for portable electronics and mobile technology.

---

[a] Author to whom the correspondence should be addressed. E-mail: sanju.gupta@wku.edu.

While solar and wind energy sources are intermittent, a continuous plentiful and large scale electrical energy supply will only be possible if inexpensive storage and conversion systems are developed. Of primary interest to us in recent years have been electrochemical energy conversion and storage devices including supercapacitors, pseudocapacitors and batteries, which represent efficient and environmentally benign technologies. Each of these systems as described in Ragone plot offers different characteristics in terms of specific power and energy densities.[2] For instance, rechargeable secondary Li-ion batteries can have high energy densities with low power densities and electrochemical supercapacitors can deliver very high power density with a lower stored energy than batteries, but rapid charging/discharging, superior cycle lifetime and high reliability. Accordingly, supercapacitors are particularly appropriate for applications where high power is needed for a few seconds (*e.g.* for power buffer, power saving units and energy recovery).[1] They can complement Li-ion batteries in applications where both high energy and high power delivery/uptake be achieved. These characteristics originate from the driving mechanisms which govern how energy is stored in the batteries and supercapacitors. Accordingly, the supercapacitors, known as electrochemical double layer capacitors, store charge at the surface of the electrodes that is at the electrode-electrolyte interface through reversible ion adsorption thus charging a ‘double-layer’ capacitance typically made from carbon-based materials.[2–4] This particular mechanism differentiates them from batteries, which involves actual electron transfer in electrochemical redox reactions and resulting structural modification due to Li-ion intercalation/de-intercalation to produce electrical energy. To increase the charge storage capacity in supercapacitors, it is necessary to increase the electrodes surface area. While there is no linear relationship between the surface area and the gravimetric specific storage capacity, we employ innovative synthetic methods and strategic approaches to address challenges of achieving both the high specific and specific power densities concomitantly. As a result, we consciously develop ‘hybrid’ supercapacitors or pseudocapacitors,[5–8] which involves surface redox (Faradaic) reactions like in batteries. The catalyst community is also drawn towards the development of these electrochemical electrodes as advanced electroanalytical platforms seeking potential game changers with novel means of turning abundant materials into cost-effective active catalysts with favorable mechanistic pathways to extend lifecycle. It seems paramount that nanoscale materials with exceptional electrochemical (re)activity, selectivity and stability are needed to meet the demanding performance in renewable energy sector.[9–11]

Graphene, two-dimensional structure of carbon atoms packed into a dense honeycomb crystal, has attracted a great deal of interest due its diverse and fascinating properties including high gravimetric surface area (*ca.*2,630 m^2/g), superior charge-carrier mobility ($2x10^5$ $cm^2/V.s$), excellent tensile strength 130 GPa, and thermal conductivity $(4.84\text{-}5.30)x10^3$ W/m.K.[10,12] Of several methods,[13] chemical production of graphene is currently the lowest cost method and it is becoming a preferred method for large-scale production, that are also used to produce graphene variants namely, graphene oxide (GO), and chemical reduced GO (rGO) and electrochemical reduced GO (ErGO).[11,14–16] Few-layer GO nanosheets are lesser conductive as they contain significant number of oxygen-rich functional groups favoring surface and edge decoration and abundant crystallographic defect densities.[10] In view of exceptional physical-chemical properties, the functional groups offer rich surface chemistry as they are considered ideal support for chemical bridging and molecularly anchoring various metal and metal oxide nanocrystals to form high-performance functional nanocomposites as ‘hybrid’ supercapacitive electrodes.[17–20] The manufacturing of such hybrids require that these metal oxide nanoparticles be incorporated and homogeneously distributed on graphene nanosheets. Additionally, the graphene supports (especially, rGO and ErGO) is promising for direct conductive path for rapid electron transportation. Numerous studies have been reported in the last few decades related to transition metal oxides including RuO_2, V_2O_5, Fe_3O_4, MnO_x and Co_xO_y as they represent the most fascinating class of inorganic materials for wide ranging physical and chemical properties. The growing interest in cobalt and manganese oxides stem from their emerging applications in solid oxide fuel cell (SOFC) and heterogeneous catalysis. Similar to iron and copper, manganese (Mn^{2+}, Mn^{4+}), vanadium (V^{2+}, V^{3+}, V^{5+}) and cobalt (Co^{2+}, Co^{3+} and Co^{4+}) exhibit multiple oxidation states and intermediate valences with charge ordering phenomenon. Moreover, their extraordinary capability to adopt several coordination and structures with tetrahedral, pyramidal to octahedral sites makes them exceptionally attractive. Additionally, various dimensionalities (1D, 2D or 3D) allow great flexibility of the oxygen framework such that non-stoichiometry (oxygen vacancies) in these compounds is crucial for tunable physical and chemical properties. The electronic structure of Co, V and Mn as compared with other 3d metals is a complex topic due to various spin states. The physicochemical properties of oxide polymorphs are coupled with structural transitions with a high complexity involving electronic (or possibly electrochemical) phase separation phenomenon. One of the other common ways of prevailing valence state is the disproportionation reaction: $2Co^{3+} \longleftrightarrow Co^{2+}+Co^{4+}$, which plays a profound role in the electrical conduction and other physical/chemical properties. The interest in electrode materials based on these metal and metal oxides for supercapacitors (or pseudocapacitors) is due to environmental benign nature, abundance and theoretical capacitance besides coexistent specific energy and power densities characteristics, long cycle life, wider potential window, good thermal operating range and low maintenance cost.[10,11,21–24] Therefore, hybrids based on nanostructured Co and Mn oxide polymorphs onto graphene supports provide an excellent model for in-situ Raman spectroelectrochemistry investigations, not so abundant in the literature. Alternatively, multifunctional hybrid electrodes assembled with strongly coupled organic (nanocarbon)−inorganic interfaces promote effective surface charge transfer and faster electron/ion transport (charging−discharging).[10,11,25–27]

At a fundamental level, the *electrode-electrolyte interface* is the energy storage system that defines the performance of diverse electrochemical devices with applications related to energy (conversion and storage), water (purification and remediation), catalytic (hydrogen and fuel cell), and (bio)chemical sensing. Thus fabrication of optimized architectures having suitable functionality requires the ability to control the interfacial composition and molecular interaction between the micro-constituents. Hence, structural characterization is fundamental and active area needed for structural optimization for applied electrochemistry. Nevertheless, the interfaces are generally less amenable to standard surface-science characterization methods, making the surface activity investigation at nanoscale challenging. The prediction of properties requires identifying and quantifying salient structural characteristics, while gaining insights into the relevant mechanisms those can be achieved through in-situ observations of structural evolution. In our previous work, we reported detailed study of the synthesis, microstructure and electrochemical properties of graphene-family nanomaterials decorated with cobalt nanoparticles, cobalt oxide and manganese oxide polymorphs.[11,22] Using novel synthetic approaches, we facilitated chemical bridged interfaces via electrodeposition[10,11,22,28] and there-dimensional scaffolds by hydrothermal (HT) method.[10,11,29] We demonstrated that Co_3O_4-based hybrids on electrochemically reduced graphene oxide (ErGO), on multilayer graphene (MLG) and with rGO_{HT} and nanostructured MnO_2 on GO are capable of delivering maximum gravimetric specific capacitance (C_s) > 550 F.g^{-1} at discharge current density 10 A.g^{-1}. We attributed these remarkable findings to (a) interplay of open pore graphene network beneficial to ion diffusion and transport kinetics, (b) topologically multiplexed highly conductive pathways provided by MLG, ErGO and rGO_{HT} support to ensure rapid transfer and electron/ion conduction (< 10 ms) and (c) optimized loaded inorganic nanomaterials on graphene nanosheets prohibiting aggregation. Computational simulations *via* periodic density functional theory (DFT) with and without transition metal adatoms on graphene and GO sheets were performed to synergize and complement experimental work. Beyond the encouraging results we reported and the limitations observed, fundamental mechanistic understanding of energy storage (ion adsorption, electron transport and charge transfer) in organic-inorganic hybrids has yet to be established.

Among various complementary techniques (*i.e.* X-ray diffraction, electron microscopy, optical spectroscopy, neutron scattering), vibrational spectroscopy provides unique structural information at a molecular scale. Raman spectroscopy (RS), a simple and nondestructive surface-sensitive inelastic light scattering technique, proved to be versatile for a vast array of carbon-based nanomaterials and found to be responsive to the state of chemical bonding for metal oxides, with the Raman frequencies being dependent on the metal oxidation state. Moreover, microphases observed under the microscope allow the characterization of structural phase transitions and identification of polymorphic forms. Since the Raman probe is capable of studying highly localized volumes with dimensions comparable to the grain size, they become significant for nanoengineered electrochemical electrodes. In addition, the use of Raman imaging enables to map accompanying electrochemical bias-induced transformed zones and microscale homogeneity through the observation of specific vibrational modes. To promote such developments, the in-situ Raman spectro-electrochemistry investigations of graphene-transition metal oxides 'hybrids' are reported. The nanostructured transition metal oxides including manganese and cobalt oxide polymorphs decorated graphene-family nanomaterials (GFNs) form viable frameworks for rationalizing the electrochemical activity trends via probing lattice vibrational structure under applied bias providing fundamental underpinnings of charge transfer dynamics and elucidating structural stability in carbon-metal-oxygen triad electrochemistry. The experimental findings complemented with density functional theoretical calculations can be predictive for expansive rational design of compositional interfaces and reactivity space for next-generation 'hybrid' electrodes and sensing platforms. The combined experimental and theory provides a wealth of new information about the physical-chemical processes at solid/liquid interfacial reactions and constitutes the key findings that helps to quantify *structure-property-(re)activity relationship*s (qSPARs).

II. EXPERIMENTAL

A. Materials and methods

The electrodeposition method of graphene-based hybrids, surface morphology using scanning electron microscopy, surface binding energy using X-ray photoelectron spectroscopy and theoretical calculations using Density Functional Theory (DFT) are provided in the supplementary material.

Raman spectroscopy (RS) was performed to obtain the lattice vibrations at various points on the nanostructured transition metal oxides decorated graphene nanosheets hybrids. To acquire Raman spectra, a micro-Raman spectrometer (Model InVia; Renishaw, UK) equipped with an excitation laser of wavelength 633 nm ($E_L = 1.92$ eV) and ~0.5−2 mW incident on the sample, with edge filters cutting at ~100 cm^{-1} was used. The Raman light from the sample was collected in backscattering geometry, transmitted by a beam splitter, and detected by a CCD camera with an integration time of 60−600 s. A 2μm spot size was obtained using an objective lens of x50. An edge filter removed the laser excitation, filtering the reflected light then sent to a spectrometer. Extreme care was taken to avoid sample damage caused by laser induced thermal degradation. Raman shift ranged 200 cm^{-1}−3400 cm^{-1} for Co containing hybrids, while for cobalt oxide and manganese polymorphs, the shift was kept between 100−800 cm^{-1} and for GO, rGO$_{HT}$, ErGO, and MLG it was kept between 1150−3200 cm^{-1} with spectral resolution 1 cm^{-1}. The in-situ Raman spectro-electrochemical experiments were conducted to obtain insights into the charge transfer dynamics and energy storage mechanisms of the graphene-inorganic hybrids. We specifically custom-made two-electrode electrochemical cell integrated with Raman microscope in addition to long working distance objective lens 100x (Model Leica) which allowed to monitor Raman spectra in operando experimental conditions (see Fig. 1

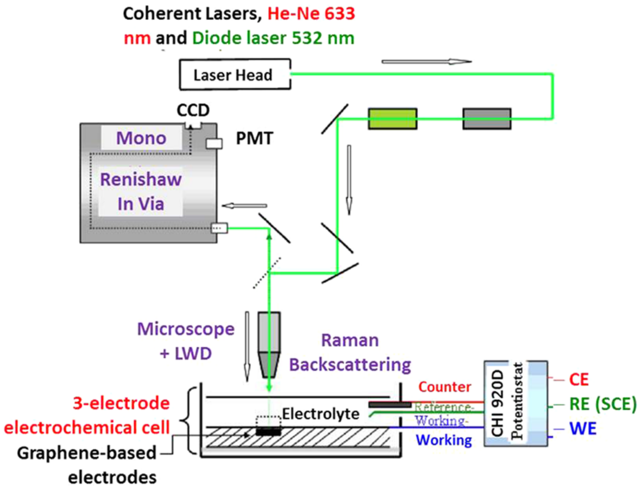

FIG. 1. Schematic of the experimental setup of in-situ Raman spectro-electrochemistry: counter, reference, and working electrodes in a single-compartment electrochemical cell and other accessories.

schematic). Since the spectra were recorded using a long working distance, the probed area was about 3 μm^2. The spectrometer slits were set at 100 μm, resulting in a resolution of ~1.0 cm^{-1} and uncertainties of 0.05 cm^{-1} or smaller in peak positions. The Raman spectra were collected in spectral window of 300–800 cm^{-1}, 1100–1800 cm^{-1} and 2450–2850 cm^{-1} under applied electrochemical potential with interval 0.1V in amperometric mode from −0.2V to +0.8V for cobalt-based (from −0.9 to +0.9V for MnO_x-based) hybrids. The PTFE cell was fixed and contained the counter electrode (Pt wire of 3mm diameter), reference electrode (Ag/AgCl 3MKCl saturated) and working electrode (samples) immersed in electrolyte 0.5M KOH for cobalt-based (in 0.1M Na_2SO_4 for MnO_x−based) oxides. The illuminating light was focused after each measurement to keep the level of intensity same throughout the experiments. The Raman spectra were measured at the end of each potential step, after waiting for the current to fall below 1μA to ensure quasi-equilibrium conditions. For each electrode, it was cycled for at least one full cycle to assess the reversibility of the charge transfer and storage capacity in cyclic voltammetry (CV) mode at 100 mV sweep rate. All of the chemicals were analytical grade and the electrolyte solution is prepared using DI water. Furthermore, Raman mapping was also measured at potentials 0.3V and 0.4V depending on the sample, measuring the corresponding Raman spectral variation over 20x20 μm^2. The spectra were fitted using in-built Raman spectrometer software Wire v.4.2 based on Marquardt–Levenberg method.[30]

III. RESULTS AND DISCUSSION

A. Surface characterization

Figure 2 shows SEM images of electrodeposited Co_3O_4, Co_3O_4/ErGO, CoO, CoO/ErGO, CoO/rGO, CoNP, CoNP/MLG, GO, rGO, MnO_x, MnO_x/GO MnO_x/rGO and hydrothermal synthesized Co_3O_4/rGO_{HT} samples. They reveal relatively uniform surface morphology, where interconnected three-dimensional (3D) network and crumpled silk-like graphene nanosheets (GNS) optimally decorated with nanocrystalline Co_xO_y, CoNP and MnO_x is apparent. The lateral size of micro/nanoparticles ranged between 50−100 nm and electrodeposition takes place preferentially at edges or on nanowalls of GNS that prevents their re-stacking. For the hydrothermal samples, many stacked nanoplatelets and scrolled GNS are observed (not shown, see Ref. 11). It is conceivable that below a critical areal density of nanostructured transition metal oxides, the GNS may aggregate decreasing the available specific surface area for ion adsorption and in turn charge storage capacity. Since electrochemical processes and electrocatalytical reactions mainly occur on the surface/interface, it is useful to investigate the surface signatures. The binding energies of core electrons measured are sensitive to chemical and structural properties of their solid-state environment.[31] Figure 3 shows wide scan XPS spectra of as-synthesized ErGO, CoO/ErGO, CoNP/MLG, Co_3O_4/ErGO and Co_3O_4/rGO_{HT} confirming the existence of C, O and Co elements in hybrid electrodes. XPS core level C1s (282-300 eV), Co2p (775-800 eV) and O1s (528-540 eV) elemental spectra provide surface chemical composition. Peak fitting using Voigt functions was accomplished to identify oxygenated functional groups considering their binding energy location in hybrids.[32] The C1s spectrum of ErGO exhibited four peaks centered at positions 284.9, 287.9, 292.5 and 295 eV assigned to C-C//C=C, C-O, C=O, C-OH/O-C=O, -COOH, respectively and shake-up satellite peaks. As seen in Fig. 3, −C=O (287.9 eV) and C−C (284.9 eV) bonds are formed and increase with cobalt-based compounds, as well as carbonate ($CO3^{2-}$) (295 eV) at higher thickness. These groups are also typical of MLG, GO and rGO which can form epoxide (C−O−C), hydroxyl (−OH), carbonyl (C=O) and carboxyl (−COOH) groups both on the basal plane and at edge plane sites. Peaks of the C1s spectrum of various hybrid nanomaterials studied were found at similar position as for ErGO, but the C/O proportions were different. For instance, some oxide groups (C=O and C−OH) are present in lower concentration in MLG than those of GO, rGO and ErGO, which can be attributed to native oxidation and/or adsorbed water molecules. From the peak intensities of the O1s core level (531 eV) spectrum, the −OH group forming at higher Co thickness are not only due to C−OH bonding, but also it occurs due to formation of Co[OH]2 or divalent ionic state of Co^{2+}. Therefore, Co 2*p* XPS spectrum is examined further in detail (see Fig. 3). There may also be a contribution from cobalt

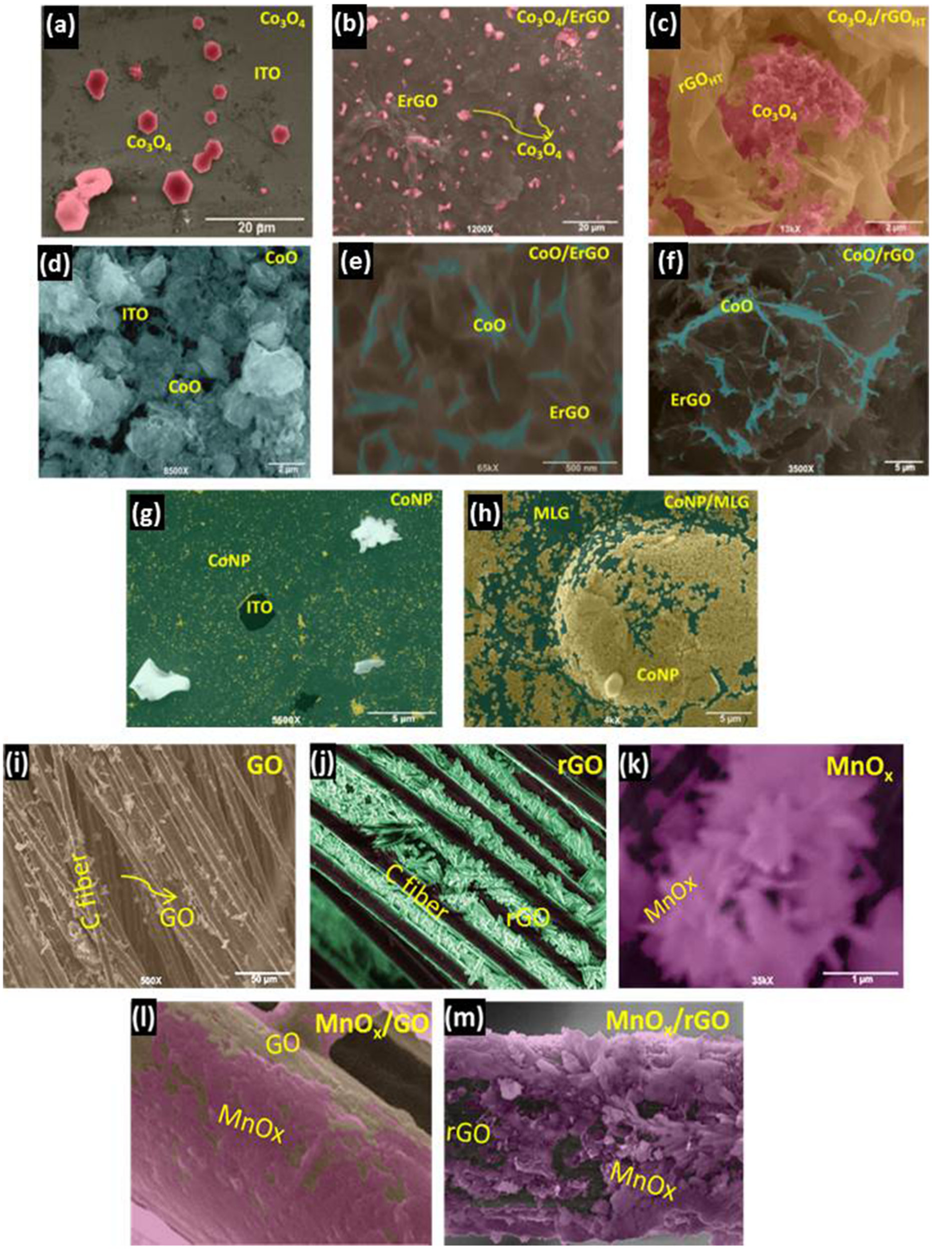

FIG. 2. Scanning electron microscopy images of representative electrodeposited graphene-based hybrid samples consisting of graphene-family nanomaterials and (a-h) cobalt–oxide polymorphs (Co_3O_4 and CoO) and (i-m) manganese oxide (MnO_x). These images are falsely colored to emphasize individual components as labeled. (Scale bars are shown at the bottom of the images).

oxides at the O1s peak in the spectral range 531−534 eV. The spectrum contains three main peaks at 531.1, 532.6, and 533.8 eV attributed to Co−O (metal-oxygen) and Co−O−H, H−O−H and O−C (reduction), respectively. Typically, the oxygen content increase is proportional to the thickness of electrodeposited cobalt oxides.

Figure 3 also shows two Co 2p peaks relating Co $2p_{1/2}$ (~795 eV) and Co $2p_{3/2}$ (~780 eV) spin-orbit peaks. To probe the electronic states, the Co2*p* spectra in hybrids were fitted for deconvolution, in which the two peaks have different oxidation states which are Co $2p_{3/2}$ having Co^{3+} (*ca.* 780.6 eV) and Co^{2+} (*ca.*778.9 eV) states. Comparison of Co/Gr/Cu samples with Co islands to $Co[OH]_2$ reference shows good agreement with the lineshape and charge transfer satellites which are typical

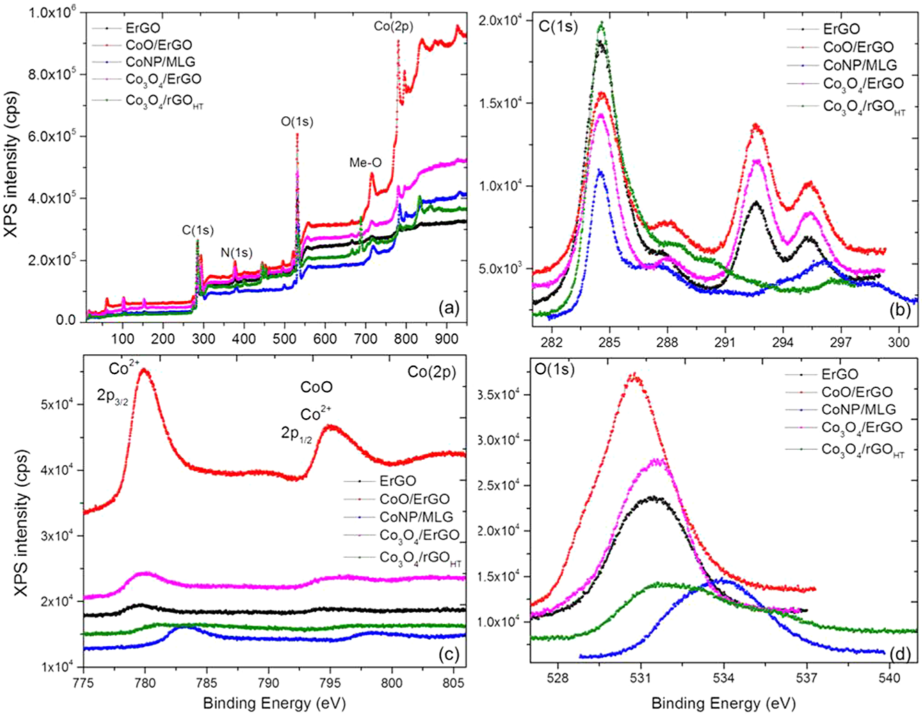

FIG. 3. (a) Typical XPS survey spectra (0–1000 eV) for one of the representative graphene-based hybrid samples consisting of graphene-family nanomaterials and cobalt oxide polymorphs and CoNP depicting the dominant elemental C1*s* peak (284.5 eV) along with the O1*s* (531.0 eV) and Co2*p* (780.0 eV) peaks. Also shown are high-resolution XPS spectra for (b) C1s (c) Co2p and (d) O1s core level peaks.

for Co^{2+} spectra.[33] The Co $2p_{3/2}$ and Co $2p_{1/2}$ peak exhibit an energy splitting ($\Delta E = 16.1$ eV) also consistent with Co^{2+} state.[34,35] The ratio Co^{2+}/Co^{3+} in Co_3O_4-based hybrids are calculated to be 3.1 indicating Co^{2+}–rich phase. This result suggests that surface oxygen vacancies are generated during electrodeposition which can be confirmed by fine-scanned O1s XPS spectra. The spectrum of cobalt nanoparticles (CoNP) is somewhat shifted, which is attributed to a superposition of Co^0 and Co^{2+} signals in ratio 3:7. It should be noted there exists shift of Co^{2+} features between thin and thick Co layers. The presence of Co 2p3/2 peak at 780.6 eV for thin Co, blue shift (782.1 eV) is observed for thicker Co (*e.g.* Co_3O_4/rGO_{HT}), causing 2p3/2,1/2 splitting reduced to 14.6 eV. This observed shift in Co^{2+} feature to higher energy is consistent with initial formation of mostly CoO phase, partially converting to $Co[OH]_2$ which has marginally higher binding energy.[36] At lower Co thickness, the Co islands form primarily CoO with no evidence of metallic Co and for thicker Co the bottom layers in contact with the graphene (MLG) surface remain metallic Co and in contact with functionalized graphene (GO, rGO, ErGO) forms cobalt oxides.

Micro-Raman spectroscopy (RS) is used for lattice vibrational bonding characterization. Figures 4a–4h display Raman spectra in the spectral region 150–3100 cm^{-1} for representative Co_3O_4, CoO, CoNP, Co_3O_4/MLG, $Co_3O_4/ErGO_{anneal}$, $Co_3O_4/ErGO_I$, Co_3O_4/rGO_{HT}, CoNP/MLG, CoNP/ErGO, CoO/rGO, MnO_x/rGO and MnO_x/GO samples along with GO and rGO nanosheets. For a realistic comparison, the spectra are normalized to intense band at ~1595 cm^{-1}. Keeping in view of microscopic structure-property correlations, the features in Raman spectra are quantitatively analyzed and summarized elsewhere.[10,20,22–24,37] The barely visible peaks appeared for nanoparticle-decorated graphene samples and the increase in intensity ratio of D to G band strongly suggests that defects are formed at the interface between the metal oxide nanoparticles and graphene during electrodeposition. Here we provide description relevant for the current in-situ study. In Figs. 4a, 4c, 4f and 4h, the peaks at 188, 460, 515, 630 and 676 cm^{-1} are assigned to F_{2g}, E_g, F_{2g} and A_{1g}

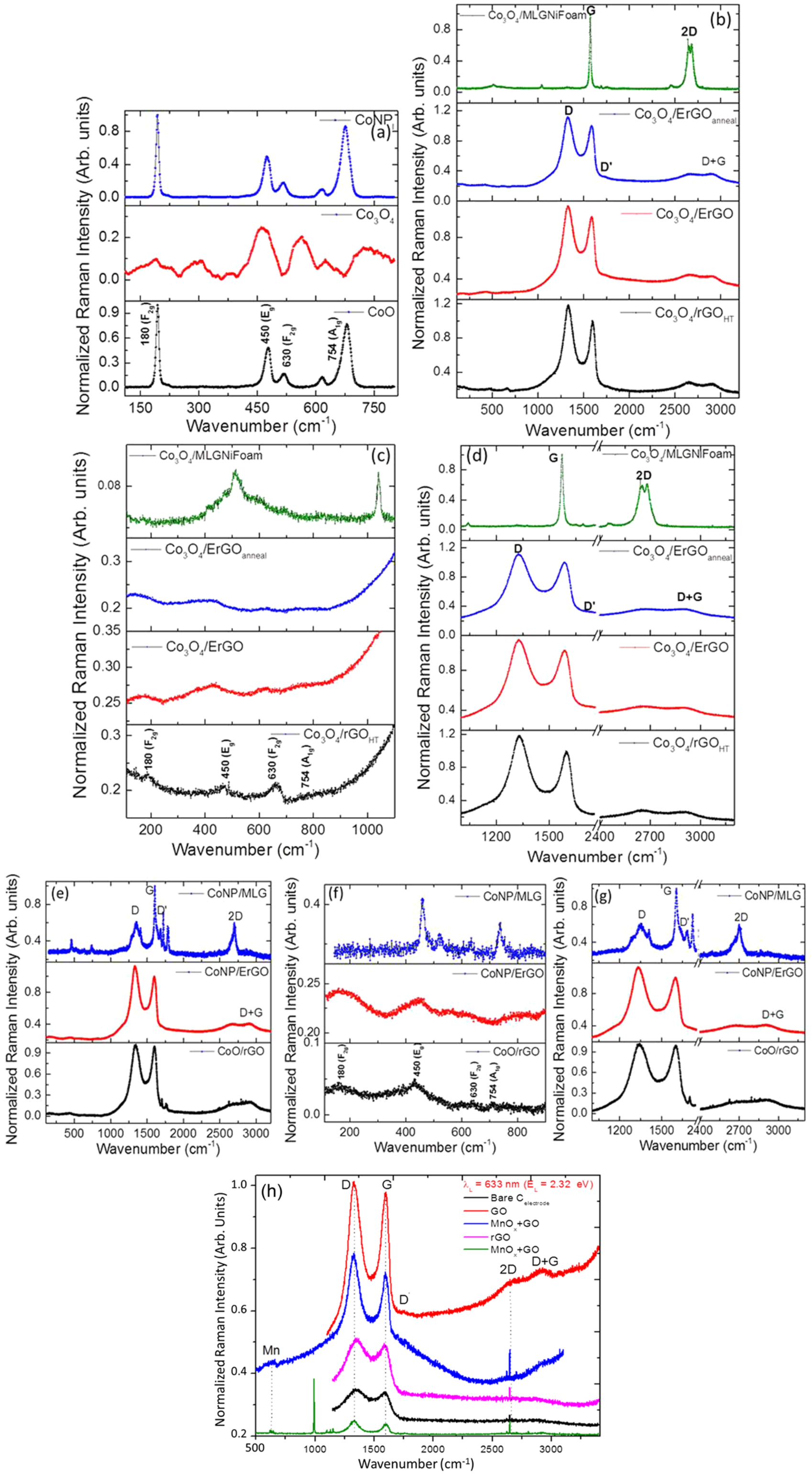

FIG. 4. Micro-Raman spectra excited at λ_L = 633 nm (E_L = 1.92 eV) in 120–3200 cm^{-1} spectral window of (a) cobalt oxide polymorphs and CoNP constituents, representative (b-g) electrodeposited and hydrothermal deposited graphene-based hybrids (Co_3O_4/MLGNiFoam, Co_3O_4/ErGO$_{anneal}$, Co_3O_4/ErGO, Co_3O_4/rGO$_{HT}$, CoNP/MLG, CoNP/ErGO and CoNP/rGO showing characteristic peaks associated with (c) cobalt oxides and (d) (D, G, 2D and D+G bands) associated with graphene nanosheets and (h) graphene-based hybrids (MnO_x/GO, MnO_x/rGO) along with bare carbon cloth substrate, GO and rGO depicting characteristic peaks.

symmetry modes, respectively, for Co_xO_y and CoNP.[10,44] The difference in the band position for CoO (rock salt), CoNP (hexagonal close packed) and Co_3O_4 (normal spinel structure with Co^{2+} in tetrahedral and Co^{3+} in octahedral interstices) is attributed to the crystal structure and level of oxygen or more appropriately, the elemental ratio *i.e.* C to Co and Co to O. Likewise, Raman spectra for MnO_2/GO and MnO_2/rGO hybrids consist of collective vibration mode associated with MnO_2 octahedron.[38,44] In our data, MnO_2 has three features at ~440 cm^{-1} and feeble doublet ~585 cm^{-1} and ~640 cm^{-1}. The band at ~585 cm^{-1} observed in Ref. 39 is assigned to Mn-O lattice vibration in MnO_2, which is in good agreement with the bulk tetragonal MnO_2 phase.[24,40,41] The band 650 cm^{-1} has E_{1g} symmetry where the stretching mode of O-Mn–O bond in MnO_6 octahedral shared by corners and/or edges in its rutile or open crystal structure with "channels".[40,41] The peak at lower wavenumber correspond to the deformation modes of the metal–oxygen chain of Mn–O–Mn in the octahedral lattice. As the manganese atom is about five times heavier than the oxygen atoms, the vibrations of the Mn–O groups are supposed to involve mainly the oxygen atoms. The characteristic diagnostic peaks for graphene are centered at ∼1360 cm^{-1} (disorder-induced D band arising due to breathing mode of aromatic rings with six fold A_{1g} symmetry) and ∼1595 cm^{-1} (in-plane stretching or tangential G band having E_{2g2} symmetry at Brillouin zone center). The other peaks of interest include second-order peaks at 2670 cm^{-1} and 2920 cm^{-1} assigned to 2D band (involves phonons near the K point) and combination D+G band, respectively (see Figs. 4b, 4d, 4e 4g and 4h).[42–44] All of the structural characterization indicate strong coupling between GNS and nanostructured cobalt and manganese oxides. The Raman spectra also confirmed a weak interfacial charge transfer *ex situ*, which has strong influence on electrochemical reactivity.[10]

First we briefly discuss cyclic voltammetry (CV) and then in-situ Raman spectroscopy results in detail. The CV measurements were carried out to define the redox potential of cobalt and manganese ions onto graphene as working electrodes in 0.5M KOH and 0.1M Na_2SO_4 electrolytes, respectively. To determine pseudocapacitive contribution within hybrid electrodes, we also characterized exclusively supercapacitive graphene electrodes. Figure 5a shows cyclic voltammograms exhibiting redox peaks in the potential range –0.2V - +0.8V. The CVs from graphene derivatives is in stark contrast to hybrids which is nearly rectangular loop indicative of almost an ideal supercapacitor (see also Ref. 10). Specifically, all hybrid electrodes displayed well-defined pseudocapacitive behavior with two sets of characteristic redox peaks centered at -0.15/+0.01 V (cathodic I/anodic II) and +0.2/+0.4 V (cathodic III/anodic IV) related to Faradaic (redox) reactions relating the conversion between different cobalt oxidation states: oxidation of Co(II) to Co(III) and Co(III) to Co(IV) following:[10] $Co_3O_4 + OH^- + H_2O \leftrightarrow 3CoOOH + e^-$ (1), $CoOOH + OH^- \leftrightarrow CoO_2 + H_2O + e^-$ (2) and $3CoO + H_2O \leftrightarrow 3Co_3O_4 + H_2$ (3). Likewise, Fig. 5b shows the CV curves for GO, rGO, MnO_x/rGO and MnO_x/GO measured in 0.1M Na_2SO_4 electrolyte in -0.9V – +0.9V potential range. The CV curves for all the electrodes show nearly rectangular shape and characteristic mirror-image with redox peaks at +0.15V and +0.45V. The reactions corresponding to charge-discharge is the proton insertion following: $MnO_2 + xH_2O + xe^- \rightarrow MnO_{2-x}(OH)_x + xOH^- + e^-$ (4) and $MnO_a(OH)_b + xNa^+ + yH^+ + (x+y)e^- \leftrightarrow MnO_{a-x-y}(ONa_xH_y)_{b+x+y}$ (5), the variables x and y indicate the number of electron equivalents that have reacted per Mn atom.[45] The reduction of Mn^{4+} to Mn^{3+} is accompanied by a proton insertion into the MnO_2 tunnel structure, x is also the number of protons inserted. At the endpoint x+y=1 and α-MnOOH is formed. The synergistic effects of chemical bridging make use of electrostatic and chemical coordinated interactions between negatively charged functional groups of GO, rGO, ErGO and Co^{2+} (and Mn^{3+}) ions architectures, promoting tailored interfaces and tunable physical properties.[10,11,46] These results suggest that the graphene nanosheets for hybrid electrodes not only improved the electrical conductivity and mechanical stability, but also elucidate functional charge transfer-like dopants to or from cobalt-based and Mn-based nanomaterials,[23,24] which are now investigated by in-situ micro-Raman spectroscopy.

B. In-situ Raman spectroscopy studies

In-situ Raman spectroscopy characterization are carried out to gain further insights into fundamental underpinning of physico-chemical processes, dynamical charge transfer and energy storage mechanisms for graphene-based hybrids, yet to be established.

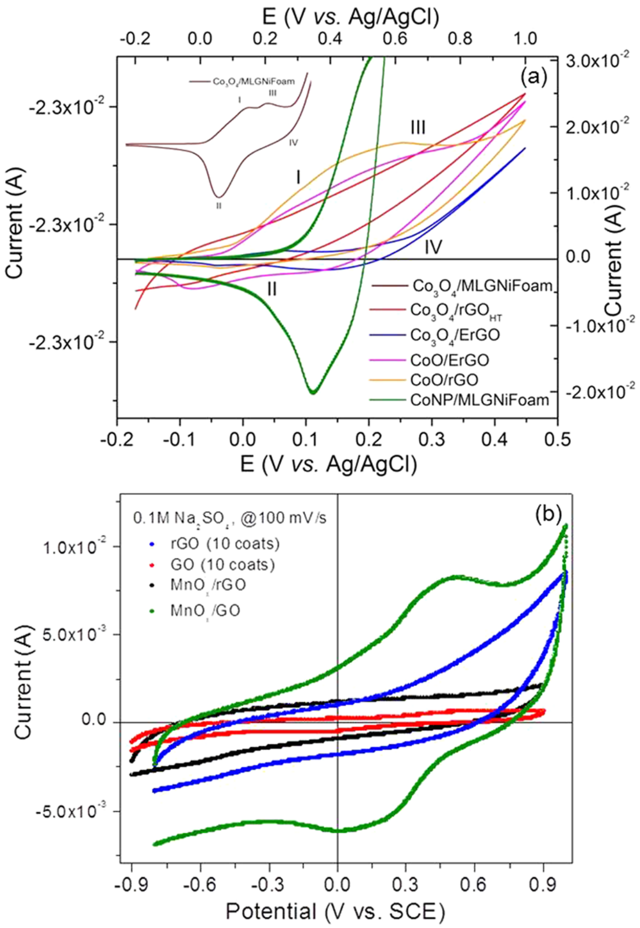

FIG. 5. Cyclic voltammograms (CV) of (a) Co_3O_4, CoO and CoNP based hybrids measured in 0.5M KOH and (b) of MnO_x-based hybrids in 0.1M Na_2SO_4 showing pseudocapacitive behavior. The inset shows CV plot of Co_3O_4/MLGNiFoam hybrid.

1. Graphene hybrids with nanostructured cobalt and manganese oxide polymorphs and cobalt nanoparticles

Assignment of the vibrational features in the Raman spectrum is carried out following Refs. 23 and 24. Prior to beginning in-situ experiments, we made an attempt if there was any change in the prominent Raman bands position and intensity when the electrodes are immersed in aqueous electrolyte. Figure 6 (panels a–e) shows deconvoluted Gaussian and Lorentzian lineshape analysis for representative examples. The Raman spectra remained almost unchanged under zero electrochemical bias except some loss in the Raman intensities that may originate from light scattering by the electrolyte solution. Figure 7 displays representative in-situ spectral evolution with bias for Co_3O_4 (Fig. 7a), Co_3O_4/ErGO (Fig. 7b–7d), multilayer graphene (MLG) (Fig. 7e), Co_3O_4/MLG (Fig. 7f–7h) from −0.2V to +0.8V, and MnO_x/GO (Fig. 7i–7j) from −0.9V to +0.9V, with respect to Ag/AgCl reference electrode. Raman spectra are normalized with respect to G band in the corresponding electrolytes. High applied bias (> +1V) were avoided because it can (a) produce tiny bubbles at the working electrode surface, which can hardly be seen by the unaided eye and may hamper inelastic light scattering collection and (b) degrade samples leading to delamination and cracking assisted by gas (H_2 and O_2) nanobubbles.

Physically speaking, when the electrodes are electrochemically polarized (either anodic or cathodic) the primary effects to be considered from Fig. 7 (and Figs. S1 and S2, supplementary material) are: (i) this process either softens or hardens the carbon-carbon bonding (d_{C-C}), which affects the

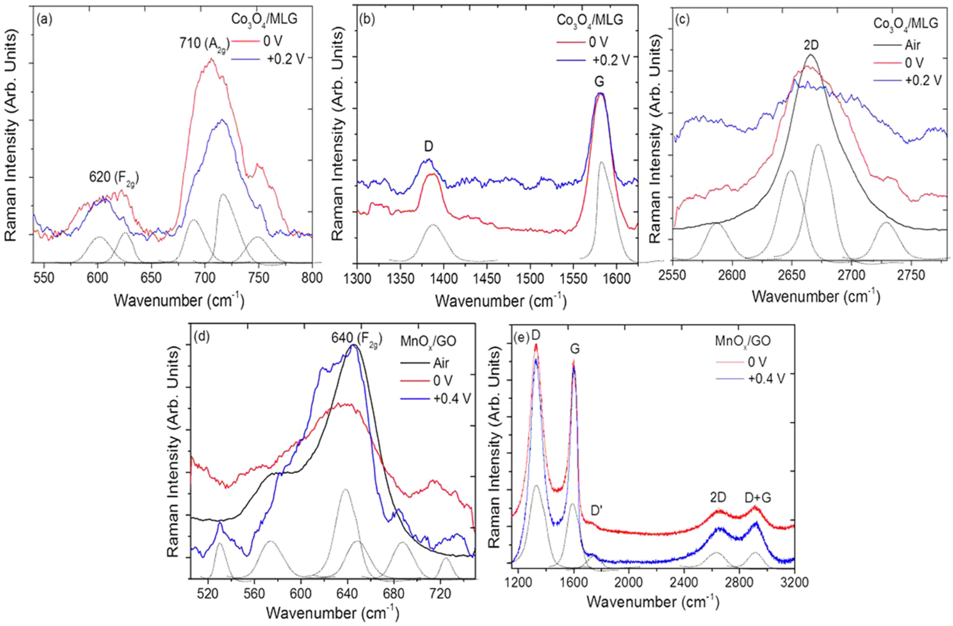

FIG. 6. Line shape analysis of characteristic Raman bands for two representative samples (a-c) Co_3O_4/MLG in 0.5M KOH aqueous electrolyte for applied potentials 0.0 V and +0.2 V and (d, e) MnO_x/GO in 0.1M KOH aqueous electrolyte for applied potentials 0.0 V and +0.4 V, vs. Ag/AgCl. The Raman spectra in air are also shown.

vibrational modes frequencies and subsequently alters the corresponding intensities of modes during early stages of charging/discharging, (ii) changes in the oxidation state of transition metal leading to structural modification, (iii) possible charge compensation of Mn^{3+} inducing a reduced state due to K^+, Na^+ and H^+ ions adsorption, (iv) solvation and hydration of graphene surface and nanostructured metal oxide nanoparticles due to intercalation of water molecules and electrolyte ions and (v) interfacial charge transfer resulting in band occupation (*n*-type) or depletion (*p*-type) resulting in shifts in Fermi level position. The first effect has some analogy with nanomaterials under hydrostatic pressure affecting the intensity and frequency of prominent Raman bands in carbon nanotubes, for example.[4] With these effects in mind, we analyzed the Raman spectro-electrochemical data.

Qualitative inspection of Fig. 7 and Figs. S1 and S2 (supplementary material) reveals the following noteworthy features: (a) decrease in D, G and 2D bands intensities especially at higher potentials, (b) changes in Raman intensities and frequency of Co- and Mn-related bands at intermittent potentials, (c) broadening or even disappearance of some Raman bands accompanies the appearance of some new bands, (d) overlap of G band with D' band that becomes active due to defects, and (e) reduction of GO and other charging/discharging process which is a quasi-reversible process, *i.e.* the changes occurring at cathodic potential excursion are not absolutely mirrored at anodic potential excursion. Figure 6 shows representative examples of the line shape analysis at two different potentials 0.0V and +0.2V (or +0.4V) vs. Ag/AgCl for Co- and Mn-based electrodes, respectively. In addition to the decrease in intensities, the number of bands required to fit with Gaussian or Lorentzian lineshape varied by at least by one band with applied potential.

It is challenging to interpret the generated data because both the cobalt and manganese-based oxides are complex materials by themselves, let alone when interfaced with multifunctional graphene-family nanomaterials in alkaline and salt solution environment in operando conditions. Nevertheless, we discuss the electrochemical potential dependent Raman spectral signatures and provide unprecedented information through detailed quantitative analysis. Figures 8–10 provide the summary of various parameters from analyzing in-situ Raman spectra with applied electrochemical potential. The variation of Co- (F_{2g} at 658 cm^{-1}; A_{1g} at 754 cm^{-1}) and Mn-related (A_{1g} at 640 cm^{-1}) high frequency longitudinal optical (LO) modes with potential for Co_3O_4/ErGO, Co_3O_4/MLG, Co_3O_4/rGO_{HT}, CoO,

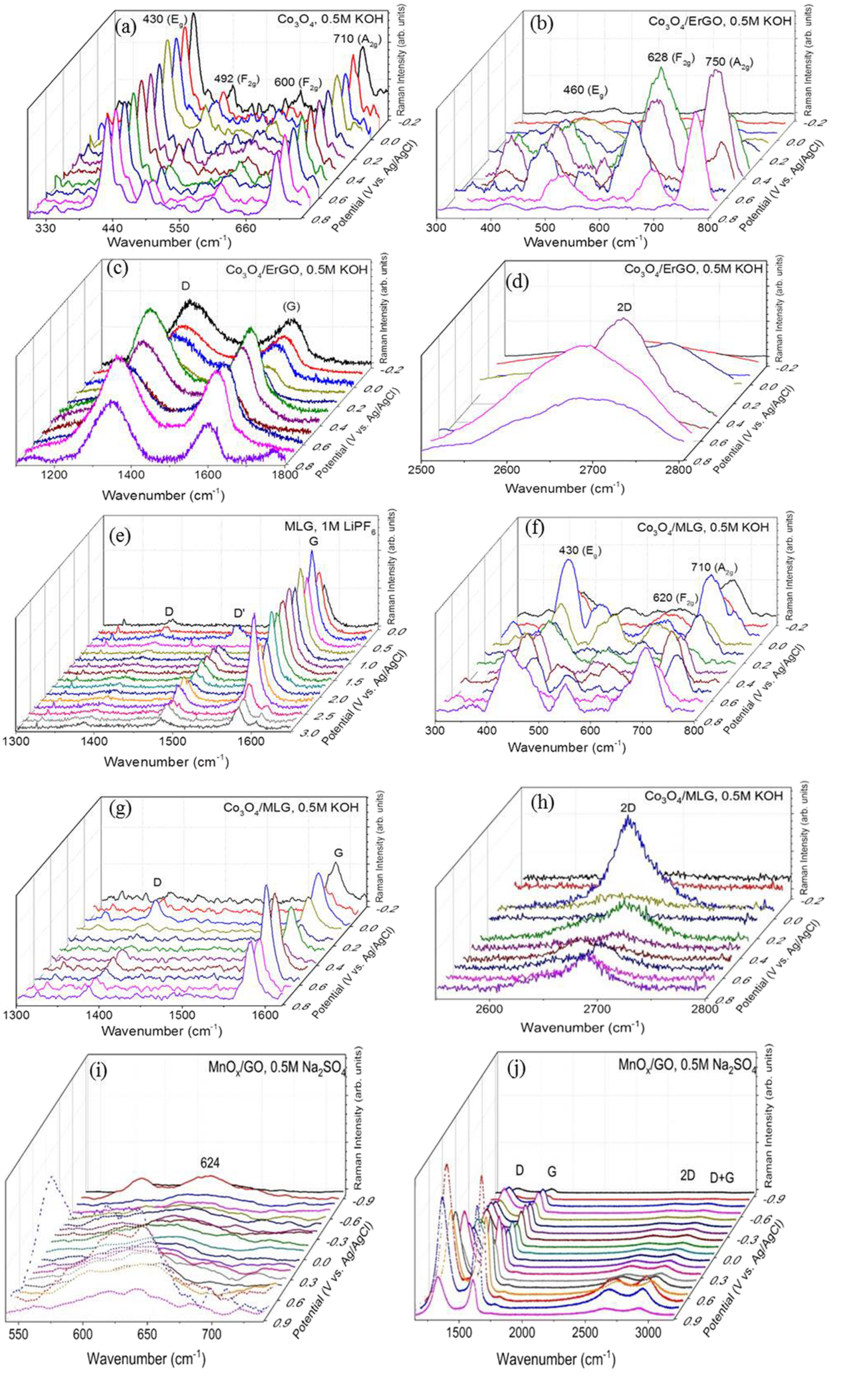

FIG. 7. Shown are in-situ Raman spectra for (a) Co_3O_4, (b-d) Co_3O_4/ErGO, (e) MLG, (f-h) Co_3O_4/MLG and (i, j) MnO_x/GO excited with laser radiation wavelength λ_L= 633 nm (E_L = 1.92 eV) in aqueous 0.5M KOH (and 0.5M Na_2SO_4) electrolytes as a function of applied potential relative to reference electrode from -0.2 to +0.8 V (and from -0.9 to +0.9V) in steps of 0.1 V from top down depicting the change in the intensity and position of various Raman bands associated with graphene and cobalt (and manganese) oxides.

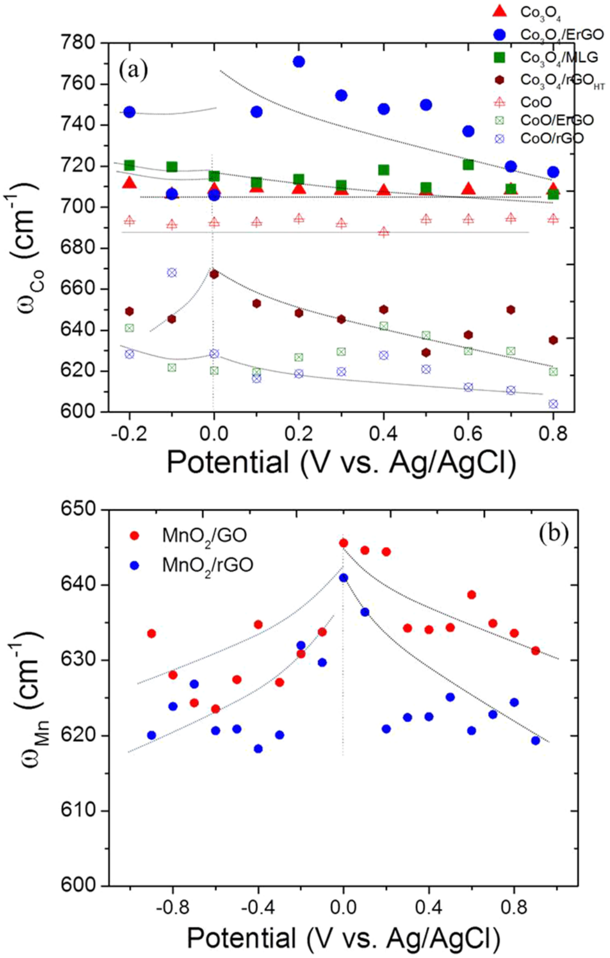

FIG. 8. Variation in frequency position (a) ω_{Co_pk1} peak and ω_{Co_pk2} peak for Co_3O_4, Co_3O_4/ErGO, Co_3O_4/MLG, Co_3O_4/rGO$_{HT}$, CoO, CoO/ErGO and CoO/rGO and (b) ω_{Mn} peak for MnO_2/GO and MnO_2/rGO with electrochemical potential relative to reference electrode. The error bars in band position are within ± 1 cm^{-1}.

CoO/ErGO and CoO/rGO, MnO_x/GO and MnO_x/rGO 'hybrid' supercapacitive cathodes is shown in Fig. 8A and 8B, respectively. In general, the A_{1g} band position decreases from 765 cm^{-1} to 720 cm^{-1} with increasing potential from +0.2V to +0.8V and to 740 cm^{-1} at -0.2V from 0V for Co_3O_4/ErGO electrodes. For most of the other Co-based samples studied the A_{1g} frequency varied from 720 cm^{-1} to 700 cm^{-1} for positive potential and almost unchanged at 720 cm^{-1} in the negative potential. As for F_{2g} mode in CoO, it varied between 690-695 cm^{-1} from 0.2 to +0.8V and it changed from 670 cm^{-1} to 630 cm^{-1} until +0.5V and then increased to 657 cm^{-1} at +0.7V with slight decrease to 650 cm^{-1} at +0.8V for Co_3O_4/rGO$_{HT}$. Conversely, for CoO-based hybrid samples, the F_{2g} mode position increases from 630 cm^{-1} to 650 cm^{-1} from 0V until +0.4V and then decreased to 630 cm^{-1} and 620 for CoO, CoO/ErGO (or 610 cm^{-1} for CoO/rGO) at +0.8V. The same band position increases from 630 cm^{-1} to 648 cm^{-1} from 0V to -0.2V. The origin of F_{2g} band in CoO can arise from Co_3O_4 due to partial oxidation, structural defects and impurities.[47] The weaker *albeit* visible TO phonon at 680 cm^{-1} and at lower wavenumber (660 cm^{-1}) come from untreated CoO and corresponding hybrids, respectively. Likewise, the position of E_{1g} band for MnO_x/GO and MnO_x/rGO fluctuated for both positive and negative potentials from 647 cm^{-1} to 635 cm^{-1} at +0.4V, from 637 cm^{-1} to 628 cm^{-1} at +0.6V, from 647 cm^{-1} to 635 cm^{-1} at -0.2V, then from 628 cm^{-1} to 624 cm^{-1} at -0.4V and gradually start to increase to 632 cm^{-1} at -0.9V.

In general, the metal and metal oxides adatoms themselves affect the electronic and structural changes. The ability of Co and Mn to adopt lower crystalline configurations such as tetrahedral

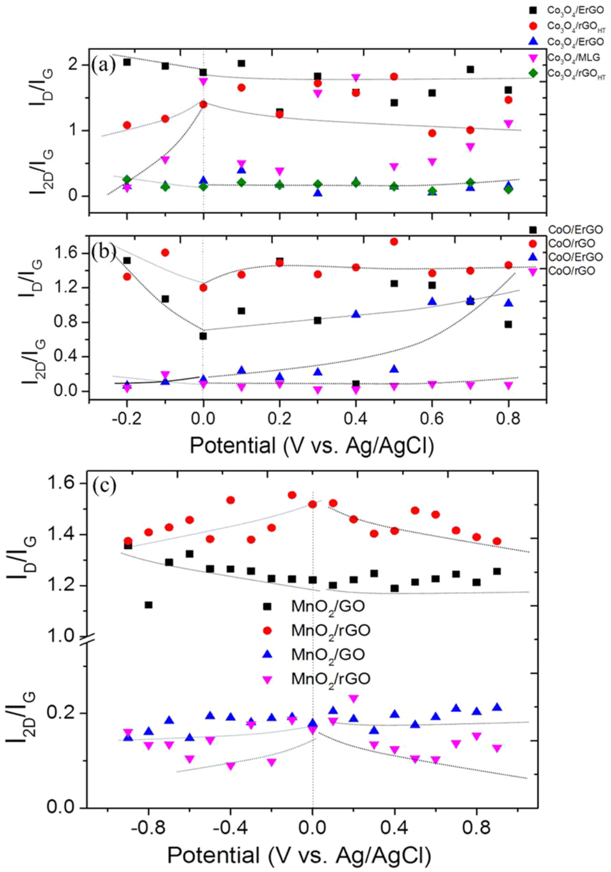

FIG. 9. Variation in intensity ratio of D to G band (I_D/I_G) and 2D to G band (I_{2D}/I_G) for (a, b) Co_3O_4, Co_3O_4/ErGO, Co_3O_4/MLG, Co_3O_4/rGO$_{HT}$, CoO, CoO/ErGO and CoO/rGO and (c) MnO_2/GO and MnO_2/rGO 'hybrid' electrodes with electrochemical potential relative to reference electrode. The error bars in band position are within ± 1 cm^{-1}.

configuration points at the oxygen vacancies that plays major role in crystal chemistries of cobaltites and manganites. Moreover, it is likely that oxidized cobalt contain mixed Co_3O_4 and CoO phases and the phonon frequencies depended upon the nanostructure size and distribution particularly when deposited on functionalized graphene (ErGO, GO, rGO or rGO$_{HT}$). Bearing in mind of the above mentioned results, it is of great interest to compare the structural evolution with electrochemical potential for distinctive Co- and Mn-based systems. Structural distortions are related to the changes in the Co−O and Mn−O bond lengths and Co−O−Co and O−Co−O bond angles, where the deviation from O−Mn−O is related to the MnO_6 octahedron distortion which is much more systematic in contrast to those associated with Co-O bonding. Furthermore, for MnO_x/GO (MnO_x/rGO) samples, the peak at 640 cm^{-1} related to Mn-O bond decreases to ~625 cm^{-1} (~620 cm^{-1}) at the highest negative potential -0.9V and to ~630 cm^{-1} (~615 cm^{-1}) at the highest positive potential of +0.9V. While different crystalline phases (or lattice structures) of transition metal oxides studied with aqueous electrochemical environment can be identified from these observations, it becomes apparent that there may be different degrees of freedom for the vibrational O-H mode due to the presence of various phases of transition metal oxides. For example, the peak shifts and the broadening of peak at 640 cm^{-1} in MnO_x–based hybrids indicate structural distortions complies with the presence of γ-MnO_2 structural phase observed from Fourier transform infrared spectroscopy.[45] It has marketable presence since it is an electrochemically active material and used popularly in alkaline batteries (primary and rechargeable versions), in pagers and photoflash sectors. It is also believed that after insertion of protons from aqueous electrolyte per γ-MnO_2, the γ-MnOOH phase forms rapidly, which is the spinel precursor closely follows the bias dependent behavior. As a result of proton insertion, the frequency

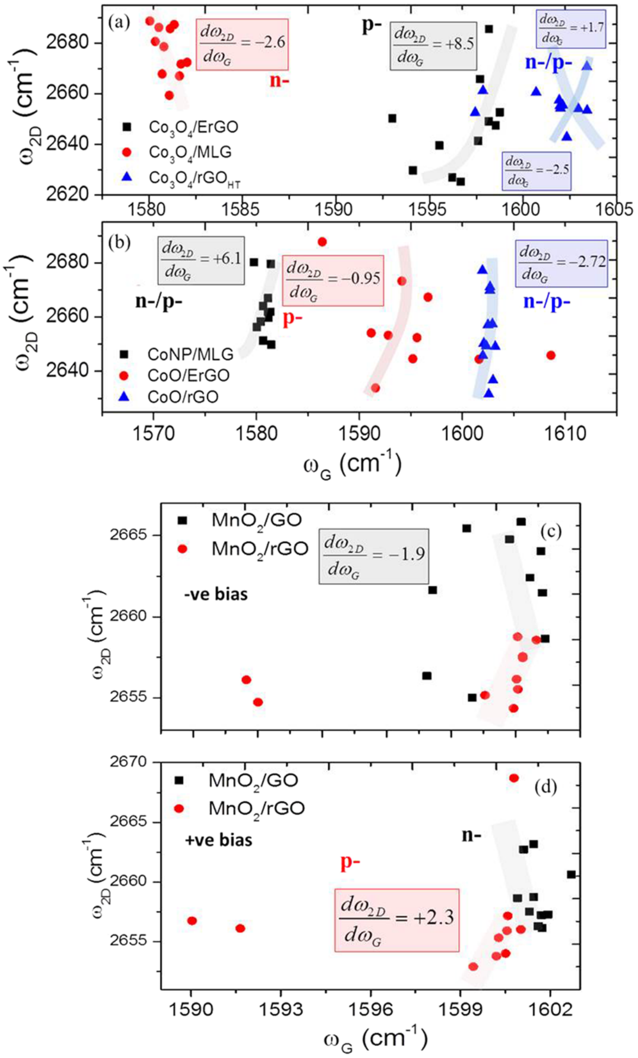

FIG. 10. Variation in frequency position of 2D band (ω_{2D}) versus G band (ω_G) for (a) Co_3O_4/ErGO, Co_3O_4/MLG, Co_3O_4/rGO$_{HT}$ (b) CoNP/MLG, CoO/ErGO, (c) negative bias window (from -0.9 to 0 V) and (d) positive bias window (from 0 to 0.9V), for MnO_x/GO and MnO_x/rGO, with electrochemical potential relative to reference electrode. The error bars in band position are within ± 1 cm^{-1}.

is shifted to lower frequency that expands the unit cell. The proton insertion starts as a single-phase reaction, with protons are inserted into the 2 x 1 tunnels of layered structure. The first evidence of MnOOH phase was due to a diffuse peak at ~649 cm^{-1} and a more pronounced peak at ~625 cm^{-1}. It is after the formation of MnOOH phase followed by lattice shearing, the carrier concentration is continually adjusted depending upon the surface coverage and nanosize as discussed. Likewise, cobalt oxide polymorphs, though weakly electroactive by themselves, becomes active when integrated with graphene and other nanocarbons. They are explored for electrochemical sensing and as advanced noble-metal free electrocatalytic platforms.[10,11]

Other aspect of the analysis is the variation in intensity ratio of D and 2D bands with G band (I_D/I_G and I_{2D}/I_G), shown in Figs. 9a–Fig. 9c, for both the cobalt− and manganese–based hybrids which They appear to be quasi−parabolic with applied bias similar to those observed for strain/stress dependence and in electrocapillary measurements on activated carbon and exfoliated graphite electrodes.[48] The ratio I_D/I_G gives a measure of aromaticity, lattice defects and restoration of graphitic domains (degree of reduction) from GO. In other words, GO reduction yielding rGO should lead to increase in I_D/I_G ratio. It is worth mentioning that we considered ratio of peak area for D and G bands instead of amplitude ratio since we observed the change in full-width at half maximum (FWHM) more than the change in peak height in most of the samples studied. We observed an increase in I_D/I_G ratio with application of bias for the GO and ErGO, which indicates the likelihood of electrochemical reduction unlike those which are already sufficiently reduced such as rGO_{HT}. In the latter somewhat opposite trend is observed. The increasing I_D/I_G ratio as the reduction proceeds suggests decreasing size of the sp^2 C domains since it is inversely proportional to the domain size (L_a). Additionally, linewidth narrowing *albeit* weakly together with G band downshift has been recently used to follow the structural ordering during the reduction process of graphene oxide as a function of applied potential.[49] Briefly, I_D/I_G changes are considered as the interplay among the degree of reduction, the C/O ratio and the generation of lattice defects. As C/O is increased, some sp^3 carbons are converted to sp^2 carbon pairs and some fraction of vacancies defects are introduced. As pairs of sp^2 C are generated, the G peak intensity increases. In addition, several sp^2 C pairs can cluster to form aromatic six-member rings which contribute to D peak intensity. For graphene layers exfoliated, sp^2 C conversion must nearly balance the number of aromatic 6-member rings formed to maintain a nearly constant I_D/I_G. According to Tunistra-Koenig (TK) relation, it is inversely proportional to L_a but this relation is valid for L_a larger than 2 nm such that the in-plane breathing mode is dampened. Upon decomposition of oxygenated functional groups due to reduction occurring randomly, we can calculate the effective distance between functional groups (*i.e.* defects) as a function of C/O using the fact that there are ~54 carbons/cm^2 of graphene surface. This leads to $L_a = (x/54)^{0.5}$, where $x = C/O$. For $x = 10$, $L_a = 0.43$ nm and does not reach 2 nm until $x = 200$. This estimate assumes that no lattice defects are formed which would break up the graphitic domains further. Chemically induced defects can also affect the 2D band behavior. The increasing trend for most of the samples studied with somewhat constant intensity (I_{2D}/I_G) ratio with applied bias for some samples studied indicate reasonable structural ordering and significantly less defect density, particular, in the hybrid samples. The occasional fluctuation (increase/decrease) with bias is possibly due to the interaction of graphene decorated transition metal oxide nanostructures leading to localized charge transfer. Despite monotonic behavior in intensities of both the G and 2D bands, the variations in Fig. 9 depict that the electron and hole injection across the π–π^* bands of the graphene-family nanomaterials is present but not ideal bipolar in nature. Alternatively, it implies that the hole and electron injection are present both in cobalt oxide- (Figs. 9a and 9b) and manganese oxide-based (Fig. 9c and 9d) hybrids. The overall decrease in intensity of these modes matches the results with those for chemical doping. Therefore, the electrochemical charging/discharging offers fine tuning of the electronic band structure.

While the number of stacked graphene layers in monolayer graphene can be identified by characteristic G and 2D Raman bands, the shifts in these band positions indicate several elements including lattice defects, mechanical stress/strain, and charge transfer to (or from) graphene sheets. Therefore, electron/hole rate rendering it makes difficult to quantitatively estimate the doping level. Recently metal adatoms and clusters on graphene have been a topic of interest and is expected that they locally dope or modify band structure.[10,23,24] In GO, the additional information is provided on the defect density and crystallite size. In order to understand further, we followed the subtle changes occurring in G and 2D bands during the electrochemical bias, Fig. 10 plots 2D (ω_{2D}) versus G band (ω_G) position. The samples experienced both upshift and downshift as marked with slopes for negative and positive potential. The band at ~1605 cm^{-1} shift toward lower wavenumbers, indicating the progressive *albeit* irreversible reduction or removal of oxygen from GO when the potential is varied from −0.2 to −0.9V and are in accord with the small currents flowing in the voltammograms at low potential. The D band also shows similar variation (not shown) in its position reported by Stankovich *et al.*[50] for electrochemical potential induced reduction. The spectra also shows upshift in G band attributed to overlap of G band with D' (~1620 cm^{-1}) band that becomes active due to defects, reduced number of sheets, resulting in blue shift similar to that observed for mechanical exfoliated graphene layers from kish graphite and the presence of isolated double bonds separated by functional groups on the carbon network of GO. The redox reactions of the different oxygen containing functional groups in GO lies very close to each other, which makes complete identification of all groups to those in in-situ measurement in aqueous electrolyte solutions. The blue shift in G band is due to non-adiabatic removal of the Kohn anomaly induced by strong electron-phonon coupling (EPC) in graphene resulting in electrochemical doping. The upshifts can be understood by considering the doping effect during discharging/charging. The stiffening of the E_{2g2} phonon with doping has been previously explained as increase in the force constant of in-plane C-C bonds similar to those observed in monolayer graphene. Interestingly, the upshift is more prominent for the graphene supports employed compared to monolayer graphene. The Mulliken charge at double bonded O atoms is higher (0.54 e) than the single bonded O atoms (0.44 e), found to be the main reason of higher binding of C=O. For carbonyl specie bonded over a tri-vacancy defected graphene sheet, we find that the linear dispersion relationship around the K-point is broken. Here conduction band minima (CBM) and valence band maxima (VBM) become broader and parabolic in nature with larger opening of band gap affecting their interaction with the metal oxides nanostructures. Nevertheless it is challenging to draw strong conclusion regarding a distinctive contribution from microscopic strain as opposed to doping by means of G band analysis. The 2D band is known to be a more sensitive indicator of strain than the G band. The apparently observed downshift of the 2D band (Fig. 10) is followed by observable loss in intensity (Figs. 5 and 6) for most of the samples studied. The intensity of the 2D band degrades by the electron-electron scattering effect, which has a positive correlation with doping level. The doping or charge transfer moved the Fermi level to a point lower than the Dirac point of graphene. The ratio I_{2D}/I_G (Fig. 9) is used to determine doping level. The decrease in this intensity ratio with G band stiffening (Fig. 10) indicates successive increase in carrier concentration in the graphene. It is highest for pristine GFNs but decreases with metal oxide decoration. Doping also leads to narrowing of the G peak (not shown), as reported by Das *et al.*[51] The stability of graphene hybrids is also apparent.

Therefore the implications are the carrier density modulation induced by charge transfer and the introduction of mechanical strain by metal or metal oxide layers. The relative strength of the G and 2D peaks' shift gives information whether charge transfer or strain effect dominates. If the shift of the G peak is much stronger than that of the 2D peak, this shift of peak is attributed to charge carrier density modulation, rather than mechanical strain. However, if the shift of the peak is caused by mechanical strain between metal oxide and graphene, the shift of the 2D peak will be much stronger than that of the G peak. In our case, the Raman peak shift is caused by the graphene charge carrier density modulation because of the relatively stronger G shift than 2D peak. Additionally, the direction of the 2D peak shift reflects the direction of the Fermi level shift. If the 2D peak is redshifted, the Fermi level of graphene moves up and graphene is expected to be doped by electrons. Alternatively, if graphene is doped by holes, the 2D peak will be blue shifted.[52] In this study, the blueshift in 2D peak for most of the cobalt oxide-based hybrids indicate hole doping. In the hybrids, electron−transfer from graphene support to Co_3O_4 occurs and Co^{3+} ions occupying the octahedral (O_h) positions are converted into Co^{2+}. Then the superexchange interactions between Co^{2+} ions at T_d (Tetrahedral) and O_h positions induce coupling of Co^{3+} (T_d)–Co^{2+} (O_h). It is also noteworthy that while Co^{3+} to Co^{2+} transformation takes place, some oxygen vacancy is also produced that could help to keep the samples electrically neutral. It should be remarked that this effect in Co_3O_4 will be restricted to very small surface regions, because the spinel structure of Co_3O_4 is unstable if a large fraction of Co^{3+} is reduced to Co^{2+} which will promote the structural transformation.[53] Likewise, for MnO_2-based hybrids, the MnO_2 octahedra interaction with constitutional water influences the structural distortion and in-turn electrochemical (re)activity. With applied bias it re-arranges water molecules in acidic media on the 'hybrid' electrode surfaces resulting in *p*-type (for positive bias) and *n*-type (for negative bias) charge transfer and hole (electron) doping is revealed (Figs. 10c and 10d). The voltage dependent G peak and 2D peak position provided complementary information for electrochemical doping of graphene, since the former is more sensitive for hole-doping, while the latter shows strong sensitivity toward electron doping. Considering the marginal G band shift value of other related doping works, *e.g.* 4 cm^{-1} by molecule doping, metal-oxide nanoparticle exhibit a more efficient doping effect, probably because of the strong chemical interactions and consequently enhanced charged transfer. The number defect density, $n_D = 1.13 \times 10^{11}$ (I_D/I_G) can also be calculated for all the samples considering point defects, bond disorder, and sp^3/sp^2 ratio in graphene nanodomains. Orbital occupancy is directly tied to band structure, such that "orbital engineering" could provide a path to controlling materials' electronic, electrochemical and optical properties. For example, control over the orbital energies and electron occupancies in Mn and Co oxides can make efficient energy storage devices, electrochromic windows and spin switches.

C. Density functional theory (DFT) calculations

Theoretical calculations have proven to be useful in predicting properties that can be difficult to deconvolute from experiments with optimized electrode-electrolyte interfaces deducing multiple charge diffusion and charge transfer events with disparate kinetics. Additional surface and interfacial effects include electrode polarization, local hybridization and electron localization, structural distortion and charge transfer attributed to ion adsorption. In this section we have carried out DFT *ab-initio* calculations that help to elucidate graphene−metal oxide and graphene oxide−metal oxide interfaces, particularly, in terms of electronic structure (*i.e.* electron density of states; DOS)[54] and localized orbital re-hybridization with (hydration/solvation effects) and without water molecules affecting electroactivity.[10,32] Figures 11 and 12 show the optimized geometries of CoO and Co_3O_4, MnO_2-graphene hydrated structures alongside comparative total and partial DOS spectra and the GO-graphene for O/C ratio ranged from 6.5% to 43.75% with and without hydration, respectively.

1. *CoO and Co_3O_4 adsorbed on graphene with and without hydration*

Non-hydrated CoO, Co_3O_4 and MnO_2 adsorbed on graphene nanosheets have been examined the report.[10] The effect of hydration on the geometry of the CoO/graphene is minimal (*i.e.* no change in the CoO height *h*, Fig. 11B) and water molecules reside relatively far from the CoO adsorbate (minimum $d_{\text{H2O-Co}} \gtrsim 3.8$ Å). The situation is different for the Co_3O_4/graphene case. Here, in the case of single water co-adsorption with the Co_3O_4 on graphene, the shortest H_2O-Co distance appears at 2.01 Å, whereas subsequent co-adsorbent water molecules are located away from the Co_3O_4 structure (Fig. 11A). Contrary to the CoO/graphene, increased hydration causes the Co_3O_4 adsorbate to be pushed away from the graphene surface and rotated (Fig. 11A). The use of larger Co basis set for the non-hydrated CoO and Co_3O_4 adsorbed on graphene show increased charge transfer from the graphene support towards the CoO and Co_3O_4 adsorbates relative to smaller basis set used in our past work.[10] Although hydration minimally affects the geometry of the CoO-graphene, the corresponding DOS spectra show that hydration alters the CoO-graphene electronic properties. More specifically, the CoO-Op DOS center-of-mass is downshifted due to hydration, in agreement with the observed charge increase for the CoO-Op orbital (Fig. 11A). However, the increased charge of the Co-d orbital due to hydration is *not* along with the upshift its center-of-mass. This effect is due to the additional states that appear near the Fermi level similar to d-band dispersion argument used for CO adsorption on Pt and PtRu clusters (see Fig. 11A and 11B).[55] This same argument can be used to explain the upshift of the Co_3O_4-Op orbital center-of-mass (*i.e.* decreased orbital population) with the increased charge of the orbital upon hydration. Figure 11B shows that hydration on Co_3O_4/graphene causes additional states to appear near and below the Fermi energy level (E_F).

2. *MnO_2 adsorbed on graphene with and without hydration*

Here we studied the effect of hydration on MnO_2/graphene. Figure 11C shows that the presence of the water molecules minimally affects the Mn atom height *h* since the water molecules appears relatively far away from the MnO_2 adsorbate ($d_{\text{H2O-Mn}} \gtrsim 3.94$ Å). We recall that for the non-hydrated MnO_2/graphene at a surface coverage of 1/8 ML, charge is transferred from the MnO_2 adsorbate towards the graphene substrate.[10] However, our current calculations are performed at the lower 1/32 ML MnO_2 surface coverage and it is found that this charge flow is reversed (*i.e.* charge flows from the graphene support towards the MnO_2 adsorbate). The reason for this charge flow change is attributed to the adsorbate-adsorbate interactions that is evident on the higher 1/8 ML coverage but is minimized at the 1/32 ML coverage. Hydration increases the charge transferred from graphene to the MnO_2 adsorbate and is due to increased charge at the MnO_2-Op orbital, in agreement with the substantial downshift of the MnO_2-Op orbital due to hydration. Similar to the VO_2, CoO, and Co_3O_4-graphene cases, the MnO_2-graphene system is metallic (Fig. 11).[10,32] Table I provides the summary of adsorbate orbital populations per atom and charge transfer to graphene substrates with one to three water molecules and without hydration.

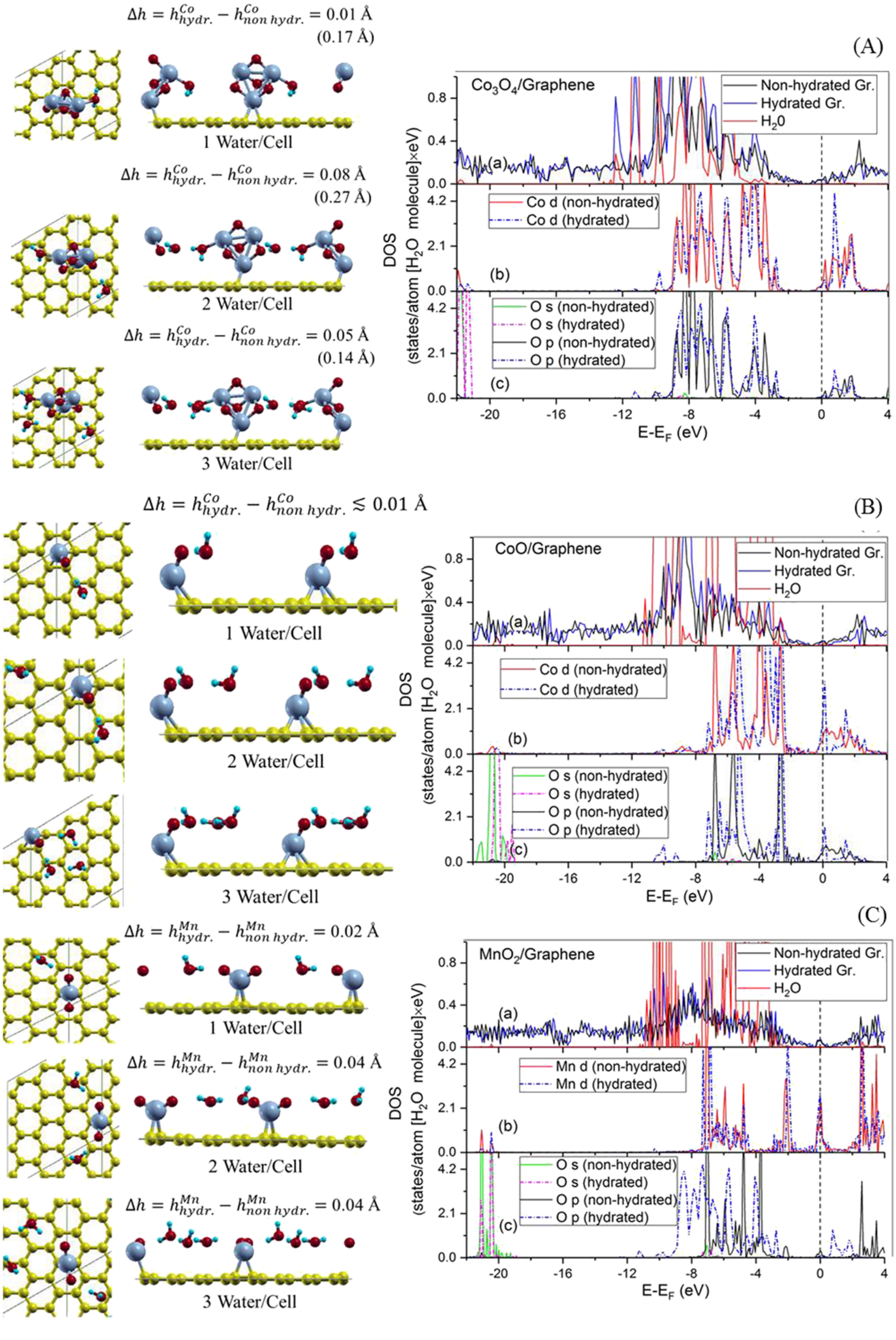

FIG. 11. (*left panels*) Schematics of optimized geometry for (a) Co_3O_4 (b) CoO and (c) MnO_2 clusters co-adsorbed with one, two, and three water molecules on graphene. The *h* values are the Co or Mn heights for adsorption on the hydrated graphene and non-hydrated graphene (closest Co or Mn to graphene). (*right panels*) DOS spectra of the (a) Co_3O_4 adsorbed on graphene with and without 3 waters per atom [H_2O] eV for a) the graphene supports of the hydrated and non-hydrated cases, b) Co d orbitals and c) the O s and p orbitals of the Co_3O_4. (b) DOS spectra of the CoO adsorbed on graphene with and without 3 waters per atom [H_2O] eV for a) the graphene supports of the hydrated and non-hydrated cases, b) Co d orbitals and c) the O s and p orbitals of the CoO. (c) DOS spectra of the MnO_2 adsorbed on graphene with and without 3 waters per atom[H_2O] eV for a) the graphene supports of the hydrated and non-hydrated cases, b) Mn d orbitals and c) the O s and p orbitals of the MnO_2. The 4×4 graphene supercell is used. The vertical line is the Fermi level (E_F).

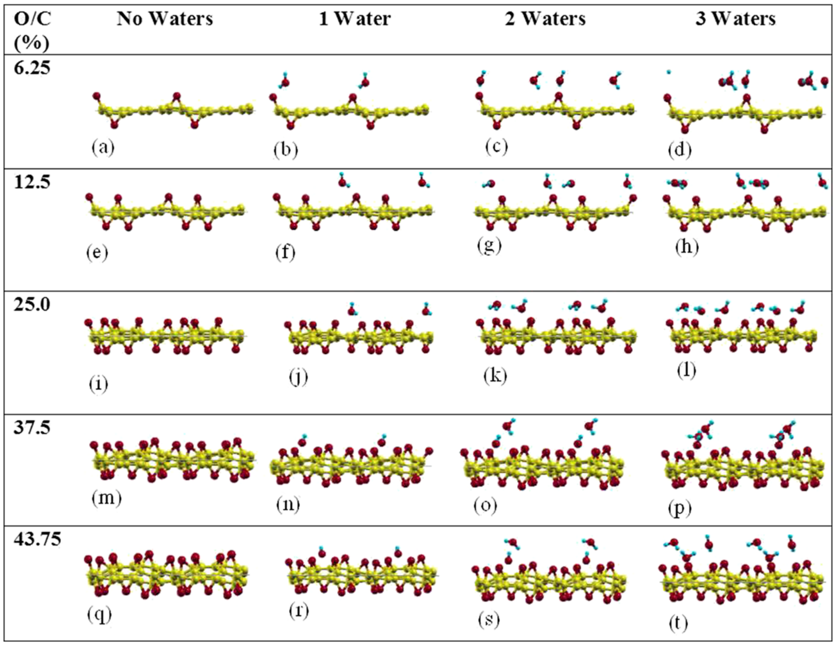

FIG. 12. Various GO-graphene hydrated (1-3 water molecules) and non-hydrated optimized structures for O/C 6.25 % (a-d), 12.5 % (e-h), 25 % (i-l), 37.5 % (m-p), and 43.75 % (q-t). The 4×4 graphene supercell is used.

3. GO-graphene with and without hydration

In our current GO-graphene calculations we examined the effects of O/C ratio in the structural and electronic properties of GO-graphene, as well as the corresponding effects of hydration relevant for this work. Figure 12 shows that the graphene out-of-plane distortions increase along with the O/C ratio. Figure 13 and Table II show the charge transfers (alternatively, doping type) from the graphene substrate towards the oxygen atoms and the water molecules (for hydrated GO-graphene).

TABLE I. Adsorbate orbital populations per atom with and without water co-adsorbed on graphene. Numbers in parenthesis refer to water co-adoption with one, two, and three water molecules.

	Charges		
Structure	Adsorbate Orbital Populations per Atom		Charge Transferred to Graphene Substrate
Co_3O_4/Graphene	Co-4s = 0.20 *e* (0.17 *e, 0.20 e, 0.20 e*)		-0.53 *e* (-0.43 *e, -0.48 e, -0.51 e*)
	Co-4p = 0.40 *e* (0.36 *e, 0.36 e, 0. 33 e*)	O-2s = 1.91 *e* (1.92 *e, 1.92 e, 1.93 e*)	
	Co-3d = 7.42 *e* (7.40 *e, 7.39 e,7.39 e*)	O-2p = 4.89 *e* (4.91 *e, 4.91 e, 4.91 e*)	
CoO/Graphene	Co-4s = 0.45 *e* (0.45 *e, 0.44 e, 0.43 e*)		-0.56 *e* (-0.69 *e, -0.76 e, -0.85 e*)
	Co-4p = 0.64 *e* (0.63 *e, 0.62 e, 0,62 e*)	O-2s =1.95 *e* (1.96 *e, 1.96 e, 1.97 e*)	
	Co-3d = 7.76 *e* (7.79 *e, 7.79 e, 7.81 e*)	O-2p = 4.70 *e* (4.76 *e, 4.79 e, 4.83 e*)	
MnO_2/Graphene	Mn-4s = 0.33 *e* (0.34 *e, 0.34 e, 0.34 e*)		-0.20 *e* (-0.30 *e, -0.37 e, -0.42 e*)
	Mn-4p = 0.03 *e* (0.03 *e, 0.03 e, 0.03 e*)	O-2s = 1.99 *e* (1.99 *e, 1.99 e, 1.99 e*)	
	Mn-3d = 5.28 *e* (5.28 e, 5.28 e, 5.28 e)	O-2p = 4.73 *e* (4.76 *e, 4.77 e, 4.78 e*)	

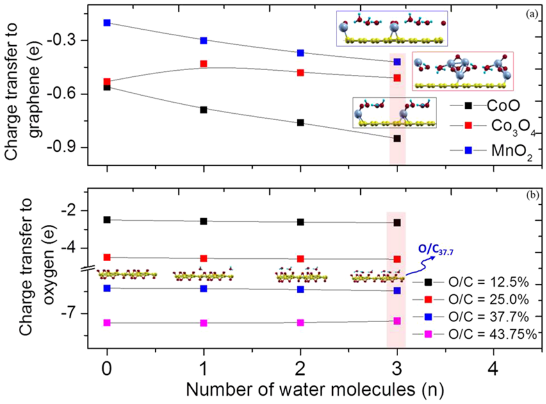

FIG. 13. (a) Charge transfers to graphene support for hydrated and non-hydrated Co_3O_4-, CoO- and MnO_2 and (b) charge transfer to oxygen for hydrated and non-hydrated GO-graphene with O/C = 12.5 %, 25 %, 37.5 %, and 43.75 %.

For the non-hydrated GO-graphene, the charge transferred from graphene towards oxygens increases almost proportionally with the O/C ratio. The GO-graphene has been examined in our last report[10] using a 2×2 graphene supercell with 8 carbon atoms per unit cell (O/C = 25 %), with the charge transfer from graphene towards the oxygen atoms reported at 1.13 *e*. If we scale this value for use on the 4×4 supercell with 32 graphene carbon atoms, then it is very close to our current value with the same O/C % (Table II). For all of our GO-graphene structures with O/C < 43.75 %, the charge transfer from the graphene support towards the oxygen atoms, and in the case of hydration towards the water molecules, increases along with the hydration. However, for O/C = 43.75 %, increased hydration leads to decreases in the charge transfer from the graphene support. This change is better understood by examining the DOS spectra of the GO-graphene with and without three water molecules (Fig. S3, supplementary material). At O/C = 43.75 %, the water molecules DOS is upshifted in energy and partially depopulated leading to decreased charge in the waters opposite to what is observed in all the other cases (see Fig. 13 and Fig. S3, supplementary material). We observe that increased GO-graphene O/C ratio increases the GO-graphene band gap, leading to insulating GO-graphene structures for O/C > 25 %. Therefore reduced form of graphene such as chemical (rGO), thermal (rGO_{HT}) or electrochemical (ErGO) reduced GO are favorable supports for electron

TABLE II. Charge transfers to graphene for hydrated and non-hydrated GO-graphene at various O/C ratios. Values in square brackets refer to oxygen surplus charges and values in regular brackets refer to water charge surplus.

	Charge transferred to graphene (*e*)			
O/C (%)	No water	1 water	2 waters	3 waters
6.25	-1.30 [1.30]	-1.38 (0.04) [1.33]	-1.45 (0.12) [1.33]	-1.49 (0.14) [1.35]
12.5	-2.49 [2.49]	-2.56 (0.04) [2.52]	-2.61 (0.08) [2.53]	-2.64 (0.098) [2.54]
25.0	-4.49 [4.48]	-4.55 (0.04) [4.50]	-4.57 (0.06) [4.51]	-4.59 (0.09) [4.51]
37.7	-6.42 [6.42]	-6.43 (0.02) [6.42]	-6.45 (0.02) [6.42]	-6.48 (0.03) [6.45]
43.75	-7.21 [7.21]	-7.22 (0.02) [7.21]	-7.21 (0.02) [7.20]	-7.17 (0.01) [7.16]

transportation while designing electrochemical energy systems. Figures 11–13 also show the charge transfers between the CoO, Co_3O_4, and MnO_2 adsorbates and the graphene support (with and without water co-adsorbents), as well as the water molecule charge surpluses and the changes of the metal oxide orbitals.

IV. CONCLUSION

In summary, we reported charge transfer dynamics using in-situ Raman spectro-electrochemistry for a series of graphene/cobalt and graphene/manganese hybrid electrodes that were strategically prepared by electrodeposition and facile hydrothermal methods facilitating chemically bridged (covalently and electrostatically anchored) interfaces with tunable properties. By virtue of crumpled and flower-like morphology, topologically interconnected mesoporous network, and the dimensionality of graphene nanosheets combined with nanostructured transition metal oxides and cobalt nanoparticles play significant role in determining the response toward electrochemical (re)activity. Additionally, controlled distribution and anchored nanostructured transition metal oxides is practically realized. The Raman spectra as a function of electrochemical bias were analyzed in terms of band position, intensity, and intensity ratio of prominent bands to quantify various processes. The key findings are: (i) the longitudinal optical (LO) phonon above 500 cm^{-1} belonging to Co_3O_4, CoO and MnO_2 and carbon-carbon bonding through D, G, and 2D bands occurring at 1340 cm^{-1}, 1590 cm^{-1} and 2670 cm^{-1}, respectively, show consistent quasi-reversible behavior and reveal structural distortions, combination of charge transfer and mechanical strain resulting in finely tuned fermi level or electronic structure due to orbital re-hybridization (ii) the Fermi level shift estimated using mathematical modeling of Raman intensity was 0.2 eV as an upper bound (iii) the changes occurred due to overlap integral between the s, p (and d) orbitals of the metal or metal oxide nanoparticles and the vicinal carbon ($\pi-\pi^*$) and carbon-oxygen atoms and (iv) the nature of charge transfer (n− or p−type). These results are complemented with DFT calculations demonstrating the synergistic coupling between hydrated cobalt (and manganese) oxide polymorphs and graphene support. It is conceivable that nanostructured transition metal oxides result in the minimization of dead volume and provision of conduction pathway by graphene support in aqueous electrolytes becomes indispensable. Finally, these findings accelerate the progress in basic understanding and we are one step closer to industrialization for future applications of graphene-based hybrids as new noble-metal free electrocatalysts for sensing platforms, rechargeable Li-ion batteries cathodes and 'hybrid' supercapacitive electrodes.

SUPPLEMENTARY MATERIAL

See supplementary material for Materials and deposition methods: preparation of graphene oxide, reduced graphene oxide, electrochemically reduced graphene oxide, cobalt and manganese oxide hybrids, description on theoretical calculations using DFT, in-situ Raman spectra: CoO, CoO/ErGO, CoNP/MLG, GO, rGO, MnO_x/rGO, DFT calculations of electron density of states (DOS) spectra: GO with and without water adsorbed at O/C = 6.25 %, 12.5 %, 25 %, 37.5 % and 43.75 %. This material is available free of charge via the Internet at http://aip.org.

ACKNOWLEDGMENTS

The corresponding author (S.G.) gratefully acknowledges financial support in parts from KSEF-RDE (Grant #148-502-17-397), KY NSF EPSCoR RSP (subaward #3200000271-17-212), KY NSF EPSCoR REG (subaward #3200000271-18-059), KY NASA EPSCoR (RID-3-NNX15AK28A, subaward #3200000029-17-229), NSF-MRI (Grant #1429563), and NSF EPSCoR Track RII (subaward #EPS-0814194) grants. The student co-author (S.B.C) is thankful to J. Andersland (Biology) for SEM and TEM training.

[1] Q. Lu, Q. Zhao, H. Zhang, J. Li, X. Wang, and F. Wang, ACS Macro Lett. **2**, 92 (2013).
[2] P. Simon and Y. Gogotsi, Nat. Mater. **7**, 845 (2008), and references therein.
[3] S. Gupta, E. Heintzman, and C. Price, J. Nanosci. Nanotechnol. **16**, 374 (2016).

[4] S. Gupta, M. Hughes, A. H. Windle, and J. Robertson, J. Appl. Phys. **95**, 2038 (2004).
[5] J. R. Miller and P. Simon, Science **332**, 1537 (2011).
[6] N. L. Torad, R. R. Salunkhe, Y. Li, H. Hamoudi, M. Imura, Y. Sakka, C.-C. Hu, and Y. Yamauchi, Chem. Eur. J. **20**, 7895 (2014).
[7] Q. Lu, J. G. Chen, and J. Q. Xiao, Angew. Chem. Int. Ed. **52**, 1992 (2013).
[8] V. Augustyn, P. Simon, and B. Dunn, Energy Environ. Sci. **7**, 1597 (2014).
[9] Q. Cheng, J. Tang, J. Ma, H. Zhang, N. Shinya, and L.-C. Qin, Carbon **49**, 2917 (2011).
[10] S. Gupta, S. B. Carrizosa, B. McDonald, J. Jasinski, and N. Dimakis, J. Mater. Res. **32**, 301 (2017), and references therein.
[11] S. Gupta and S. B. Carrizosa, Appl. Phys. Lett. **109**, 243903 (2016), and references therein.
[12] A. K. Geim and K. S. Novoselov, Nat. Mater. **6**, 183 (2007), and references therein.
[13] Y. Zhang, L. Zhang, and C. Zhou, Acc. Chem. Res. **46**, 2329 (2013), and references therein.
[14] W. S. Hummers and R. E. Offman, J. Am. Chem. Soc. **80**, 1339 (1958).
[15] S. Park, J. An, R. J. Potts, A. Velamakanni, S. Murali, and R. S. Ruoff, Carbon **49**, 3019 (2011).
[16] G. Eda and M. Chowalla, Adv. Mater. **22**, 2392 (2010).
[17] R. Holze and Y. P. Wu, Electrochimica Acta **122**, 83 (2014).
[18] S. Gupta, E. Heintzman, and C. Price, J. Nanosci. Nanotechnol. **16**, 4771 (2016).
[19] S. Gupta and C. Price, AIP Adv. **5**, 107113 (2016).
[20] S. Gupta and C. Price, J. Composites Part B **105**, 46 (2016).
[21] S. Makino, Y. Yamauchi, and W. Sugimoto, J. Power Sources **227**, 153 (2013), and references therein.
[22] S. Gupta, M. vanMeveren, and J. Jasinski, Int. J. Electrochem. Sci. **10**, 10272 (2015), and references therein.
[23] S. Gupta and S. B. Carrizosa, J. Electron. Mater. **44**, 4492 (2015), and references therein.
[24] S. Gupta, M. vanMeveren, and J. Jasinski, J. Electron. Mater. **44**, 62 (2015).
[25] X.-C. Dong, H. Xu, X.-W. Wang, Y.-X. Huang, M. B. C.-Park, H. Zhang, L.-H. Wang, W. Huang, and P. Chen, ACS Nano **6**, 3206 (2012), and references therein.
[26] X. Huang, X. Y. Qi, and H. Zhang, Chem. Soc. Rev. **41**, 666 (2012), and references therein.
[27] B. E. Conway, V. Bliss, and J. Wojtowicz, J. Power Sources **66**, 1 (1997).
[28] A. Ghosh, E. J. Ra, M. Jin, H.-K. Jeong, T. H. Kim, C. Biswas, and Y. H. Lee, Adv. Funct. Mater. **21**, 2541 (2011).
[29] J. Li, L. L. Zhang, H. Ji, Y. Li, X. Zhao, X. Bai, X. Fan, F. Zhang, and R. S. Ruoff, ACS Nano **7**, 6237 (2013).
[30] D. W. Marquardt, J. Soc. Ind. Appl. Math. **11**, 431 (1963).
[31] D. G. Castner, K. Hinds, and D. W. Grainger, Langmuir **12**, 5083 (1996).
[32] A. Hunt, D. A. Dikin, E. Z. Kurmaev, T. D. Boyko, P. Bazylewski, G. S. Chang, and A. Moewes, Adv. Func. Mater. **22**, 3950 (2012).
[33] G. H. Han, F. Gűneş, J. J. Bae, E. S. Kim, S. J. Chae, H. J. Shin, J. Y. Choi, D. Pribat, and Y. H. Lee, Nano Lett. **11**, 4144 (2011).
[34] C. D. Wagner, L. E. Davis, J. F. Moulder, and G. E. Mullenberg, *Handbook of X-ray Photoelectron Spectroscopy* (Perkin-Elmer Corporation, Minnesota, 1978).
[35] A. Lu, Y. Chen, D. Zeng, M. Li, Q. Xie, X. Zhang, and D.-L. Peng, Nanotechnology **25**, 035707 (2014).
[36] M. C. Biesinger, B. P. Payne, A. P. Grosvenor, L. W. M. Lau, A. R. Gerson, and R. C. Smart, Appl. Surf. Sci. **257**, 2717 (2011).
[37] B. R. Strohmeier and D. M. Hercules, J. Phys. Chem. **88**, 4923 (1988).
[38] F. Kapteijn, A. D. Van Langeveld, J. A. Moulijn, A. Andreini, M. A. Vuurman, A. M. Turek, J.-M. Jehng, and I. E. Wachs, J. Catalysis **150**, 94 (1994).
[39] C. Julien, M. Massot, R. Baddour-Hadjean, S. Franger, S. Bach, and J. P. Pereira-Ramos, Solid State Ionics **159**, 345 (2003).
[40] I. Rusakova, T. O. Ely, C. Hofmann, D. P.-Centurion, C. S. Levin, N. J. Halas, A. Luttge, and K. H. Whitmire, Chem. Mater. **19**, 1369 (2007).
[41] C. M. Julien and M. Massot, J. Phys. Condens. Matter **15**, 3151 (2003).
[42] K. Kobayashi, M. Tanimura, H. Nakai, A. Yoshimura, H. Yoshimura, K. Kojima, and M. Tachibana, J. Appl. Phys. **101**, 94306 (2007).
[43] M. S. Dresselhaus, G. Dresselhaus, R. Saito, and A. Jorio, Phys. Rep. **409**, 47 (2005).
[44] S. Gupta and A. Saxena, J. Raman Spec. **40**, 1127 (2009).
[45] M. Ghaemi, F. Ataherian, A. Zolfaghari, and S. M. Jafari, Electrochim. Acta **53**, 4607 (2008).
[46] M. S. Wu, Y. P. Lin, C. H. Lin, and J. T. Lee, J. Mater. Chem. **22**, 2442 (2012).
[47] Y. Li, W. Qiu, F. Qin, H. Fang, V. G. Hadjiev, D. Litvinov, and J. Bao, J. Phys. Chem. C **120**, 4511 (2016).
[48] H. Gerischer, R. McIntyre, D. Scherson, and W. Storck, J. Phys. Chem. **91**, 1930 (1987).
[49] M. Bousa, O. Frank, I. Jirka, and L. Kavan, Phys. Stat. Solidi B **250**, 2662 (2013).
[50] S. Stankovich, D. A. Dikin, R. D. Piner, K. A. Kohlhaas, A. Kleinhammes, Y. Wu, S. B. Nguyen, and R. S. Ruoff, Carbon **45**, 1558 (2007).
[51] A. Das, S. Pisana, B. Chakraborty, S. Piscanec, S. K. Saha, U. V. Waghmare, K. S. Novoselov, H. R. Krishnamurthy, A. K. Geim, A. C. Ferrari, and A. K. Sood, Nat. Nanotech. **3**, 210 (2008).
[52] W. X. Wang, S. H. Liang, T. Yu, D. H. Li, Y. B. Li, and X. F. Han, J. Appl. Phys. **109**, 07C501 (2011).
[53] Y. Y. Liang, Y. G. Li, H. L. Wang, J. G. Zhou, J. Wang, T. Regier, and H. J. Dai, Nat. Mater. **10**, 780 (2011).
[54] R. M. Martin, *Electronic Structure: Basic Theory, Practical Methods* (Cambridge University Press, 2004).
[55] N. Dimakis, H. Iddir, R. Liu, G. Bunker, R. R. Diaz-Morales, R. Liu, E. H. Chung, and E. S. Smotkin, J. Phys. Chem. B **109**, 1839 (2005).